Oxidation Catalysis of Crystalline Mo_3VO_x for the Selective Oxidation of Ethane

Ishikawa, Satoshi; Shimoda, Kosuke; Kamachi, Takashi; Aoki, Nagisa; Hagiwara, Takeshi; Urakawa, Atsushi; Ueda, Wataru

DOI
10.1021/acscatal.3c04591

Publication date
2023

Document Version
Final published version

Published in
ACS Catalysis

Citation (APA)
Ishikawa, S., Shimoda, K., Kamachi, T., Aoki, N., Hagiwara, T., Urakawa, A., & Ueda, W. (2023). Oxidation Catalysis of Crystalline Mo_3VO_x for the Selective Oxidation of Ethane. *ACS Catalysis*, *13*(23), 15526-15534. https://doi.org/10.1021/acscatal.3c04591

ACS Catalysis

pubs.acs.org/acscatalysis Research Article

Oxidation Catalysis of Crystalline Mo_3VO_x for the Selective Oxidation of Ethane

Satoshi Ishikawa,* Kosuke Shimoda, Takashi Kamachi, Nagisa Aoki, Takeshi Hagiwara, Atsushi Urakawa, and Wataru Ueda*

Cite This: ACS Catal. 2023, 13, 15526−15534 Read Online

ABSTRACT: Oxidative dehydrogenation of ethane (ODHE) is an essential reaction in modern society to produce ethylene. The orthorhombic Mo_3VO_x catalyst (MoVO) was reported as one of the best catalysts for this reaction after a particular redox treatment to generate lattice oxygen defects. This study elucidates the location and nature of the defect sites as well as how molecular oxygen is activated toward the ODHE. The insights into the active site formation and guidelines for its design were gained through structural characterization, quantification of oxygen defects, and experimental and theoretical investigation of the reaction mechanisms. Peroxo formed at the defect sites of the bridging oxygen facing the heptagonal channel was found to drive the reaction efficiently.

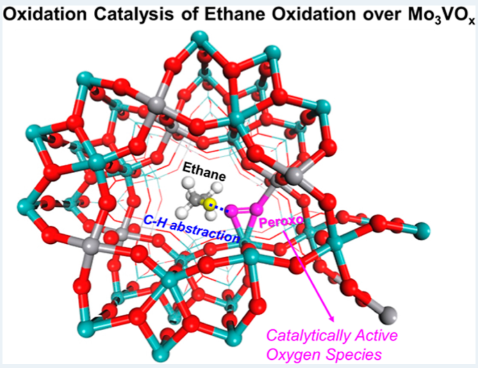

KEYWORDS: *crystalline Mo_3VO_x, oxidative dehydrogenation of ethane, micropore, active oxygen species, reaction mechanism*

INTRODUCTION

Ethylene is an important commodity chemical and is the most extensively manufactured petrochemical worldwide.[1−4] Recently, oxidative dehydrogenation of ethane (ODHE) has attracted considerable attention for ethylene production, and crystalline Mo−V−Te−Nb oxide (MoVTeNbO) is known as a state-of-art catalyst for this reaction.[1−8] MoVTeNbO consists of a network arrangement based on $\{NbMo_5O_{21}\}^{7-}$ pentagonal unit (PU) and $\{MO_6\}$ octahedral (M = Mo, V), forming hexagonal and heptagonal channels in the crystal structure, where Te = O locates mainly in the former and partially in the latter (Figure 1a).[9] As the structural analogous with MoVTeNbO, we synthesized crystalline orthorhombic Mo_3VO_x (MoVO).[10] Different from MoVTeNbO, MoVO consists of $\{Mo_6O_{21}\}^{6-}$ PU, and the hexagonal channel is partially occupied with V = O while its heptagonal channel is empty (Figure 1a).[11−13] These structural differences result in huge changes in their microporosity (Figure S1b); the adsorption property of MoVTeNbO is poor, whereas MoVO exhibits microporosity derived from the empty heptagonal channel.[8,11,14] Strikingly, MoVO demonstrates far superior catalytic activity to MoVTeNbO for this reaction (Figure S1c).[11,15]

Previously, we reported that ethane molecules enter the empty heptagonal channel micropore of MoVO and are oxidatively dehydrogenated to form ethylene and H_2O during the ODHE.[16−18] We also found that specific lattice oxygens are irreversibly removed with appropriate redox treatments from the crystal structure, which resulted in a drastic increase in the catalytic activity.[11,18,19] We speculated that the resulting lattice oxygen defects act as highly active catalytic sites around the heptagonal channel micropore. However, details of these lattice oxygen defects, including their structural sites and roles in catalysis, remain elusive. In this study, we experimentally and theoretically clarify the structural sites and catalytic functions of these lattice oxygen defects in MoVO through the direct observation of active oxygen species.

RESULTS

Generation of Lattice Oxygen Defects in the MoVO Structure. Figure 1b and Table S1 present the results of ODHE over MoVO pretreated under various conditions. Regardless of the pretreatments, the XRD patterns and external surface areas were almost unchanged (Figure S2 and Table S1). MoVO calcined under flowing air at 400 °C for 2 h (AC-1) presented an ethane conversion of 13.9% under the studied reaction condition. The ethane conversion was almost negligible when AC-1 was heat-treated at 400 °C for 2 h under flowing 5% H_2/Ar (HT-1). This inactivity was

Received: September 26, 2023
Revised: October 30, 2023
Accepted: November 7, 2023
Published: November 17, 2023

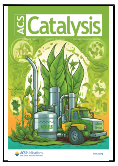

https://doi.org/10.1021/acscatal.3c04591
ACS Catal. 2023, 13, 15526−15534

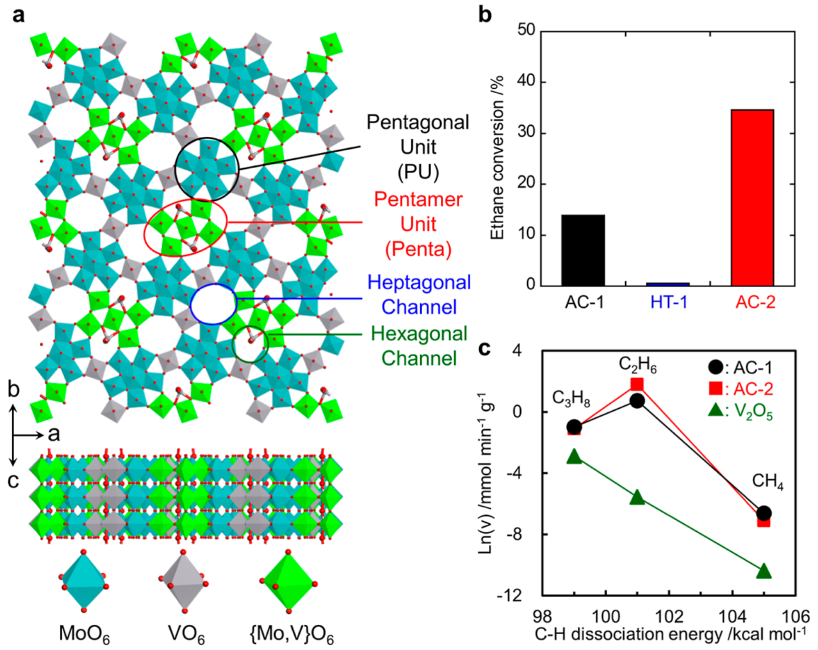

Figure 1. (a) Structural model of MoVO. VO^{2+}, located in the hexagonal channel, is represented in the "ball-and-stick" manner for better understanding. (b) Ethane conversion over AC-1, HT-1, and AC-2. Reaction conditions: reaction temperature, 300 °C; catalyst amount, 0.50 g; and reactant gas, $C_2H_6/O_2/N_2$ = 5/5/40 mL min^{-1}. (c) Reaction rate is a function of the C−H dissociation energy of alkanes over AC-1, AC-2, and V_2O_5. Reaction conditions: reaction temperature, 300 °C; catalyst amount for methane oxidation, 2.00 g (AC-1 and AC-2) or 4.00 g (V_2O_5); catalyst amount for ethane oxidation, 0.025−0.10 g (AC-1), 0.01−0.05 g (AC-2), or 0.50−2.00 g (V_2O_5); and catalyst amount for propane oxidation, 0.05−0.20 g (AC-1, AC-2) or 0.50−1.50 g (V_2O_5): reactant gas, alkane/O_2/N_2 = 2/2/21 mL min^{-1}.

attributed to the local structural changes around the heptagonal channel to prevent ethane from accessing the heptagonal channel.[11,18] By contrast, the ethane conversion drastically increased after the oxidation treatment of HT-1 (AC-2), and the ethane conversion reached a remarkable value of 34.6%.

This observation is characteristic of the ODHE. Figure 1c presents the relationships between the reaction rates of various alkanes and their bond dissociation energies (BDE). When V_2O_5 was used as the typical oxidation catalyst, the reaction rate linearly changed with the BDE of the alkane. However, the reaction rate for ethane conversion was exceptionally high over MoVO catalysts and the catalytic activity over AC-1 and AC-2 was different only in the ODHE (ODHE rate: AC-1, 2.1 mmol min^{-1} g^{-1}; AC-2, 6.0 mmol min $^{-1}$ g^{-1}; see Figure S3). It is thought that under the reaction conditions employed, only the ethane molecule could go through the heptagonal channel micropore for conversion; hence, the differences in local structures between AC-1 and AC-2 significantly affected their catalytic activity. Regarding this point, the reaction rate in methane oxidation was comparable between AC-1 and AC-2, although the heptagonal channel micropore could adsorb methane, as will be discussed later. The accessibility of methane through the heptagonal channel micropore under the adopted reaction conditions (kinetics conditions) is currently under investigation in our lab.

Previously, we identified two types of lattice oxygens in the MoVO structure.[8] One type can be irreversibly removed via reduction and barely restored via reoxidation. The other can be removed via reduction but restored via reoxidation. Herein, we denote the former oxygen as α-oxygen and the latter as β-oxygen. We previously reported that the removal of α-oxygen significantly increased the catalytic activity of the ODHE.[11,18] Hence, the location and quantity of α-oxygen defects are investigated in detail.

Figure 2 summarizes the TPR/TPO profiles of AC-1 (TPR, Figure 2a,b), HT-1 (TPO, Figure 2c,d), and AC-2 (TPR, Figure 2e,f) recorded by TCD or mass spectrometry. TPR was first conducted on AC-1 to obtain HT-1. AC-1 showed two TPR peaks: the first peak was attributed to the desorption of physically adsorbed H_2O, and the second peak was attributable to the reduction of the MoVO structure with H_2, producing H_2O through the reaction with lattice oxygens (Figure 2a,b). The corresponding weight loss was observed in the TG measurement (Figure S4a). The amount of lattice oxygen removed was determined using the second TPR peak and was 6.9/unit cell (unit cell of MoVO: $Mo_{30.2}V_{11.8}O_{114}$).[13]

Thereafter, HT-1 was subjected to TPO to obtain AC-2. There are multiple peaks that overlap in the TPO profile (Figure 2c). According to the mass profile, the first shoulder peak was assigned to the desorption of H_2O, and the following peak was attributed to the oxidation of the MoVO structure (Figure 2d). A weight gain was observed in the TG measurement during the oxidation process (Figure S4b). The amount of oxygen restored during this oxidation process was determined to be 3.6/unit cell. Based on the differences between the amount of lattice oxygen removed in TPR (6.9/unit cell) and that restored in TPO (3.6/unit cell), it is evident that 3.3/unit cell of lattice oxygen is irreversibly removed via reduction (α-oxygen).

TPR was again conducted on AC-2. In this case, the TPR profile appeared almost flat during heat treatment (Figure 2e,f). The amount of lattice oxygen removed was determined to be 3.7/unit cell. Based on the amounts of lattice oxygen removed from AC-1 (6.9/unit cell) and AC-2 (3.7/unit cell), the amount of α-oxygen was calculated to be 3.2/unit cell. This quantification result was consistent with the value estimated

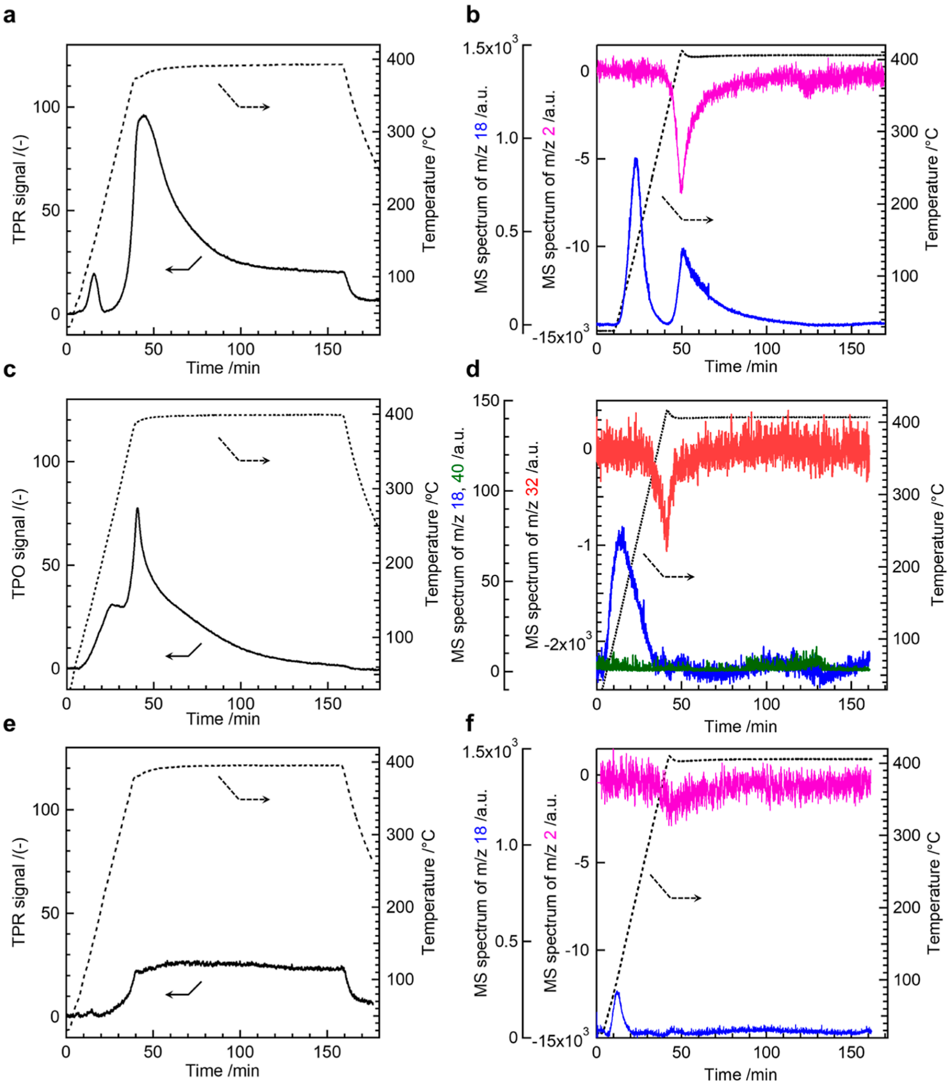

Figure 2. (a,b) TPR (a) and mass (b) profiles of AC-1 were recorded under 5% H_2/Ar flowing at 70 mL min^{-1}. (c, d) TPO (c) and mass (d) profiles of HT-1 were recorded under 5% O_2/He flowing at 50 mL min^{-1}. (e, f) TPR (e) and mass (f) profiles of AC-2 were recorded under 5% H_2/Ar flowing at 70 mL min^{-1}. $m/z = 2$ (pink), H_2; $m/z = 18$ (blue), H_2O; $m/z = 32$ (red), O_2; and $m/z = 40$ (green), Ar.

from the TPR of AC-1 and the TPO of HT-1 (3.3/unit cell). Despite the difficulty in precisely quantifying changes in the amounts of lattice oxygen during the redox treatments by the TG measurements owing to the detection limit, the amount of α-oxygen estimated based on the weight changes was 2.5−4.2/unit cell, close to those determined by the TPR/TPO experiments.

Next, neutron diffraction (ND) measurements were conducted on AC-1 and AC-2 to determine the location site and occupancy of the lattice oxygen.[20−25] Figure S5 summarizes the results of the Rietveld refinements. The simulation patterns fitted well with the experimentally obtained patterns in every case. The amounts of lattice oxygen estimated from the refined crystal structure were 111.4/unit cell for AC-1 and 108.4/unit cell for AC-2. Thus, the amount of lattice oxygen in AC-2 was 3.0/unit cell lower than that in AC-1, and the values were consistent with those determined above. The lattice oxygen showing an occupancy decrease of >5% when preparing AC-2 is marked in Figure 3a. Such lattice oxygens were concentrated within the pentamer unit (Pen). The occupancies of the lattice oxygen constituting PU and Pen in AC-1 were 99 and 98%, respectively, whereas these occupancies were 96 and 93% in AC-2, respectively. The fractions of lattice oxygen presenting an occupancy decrease of >5% when preparing AC-2 were 29% in PU and 70% in Pen, respectively. These results imply that the oxygen occupancy in Pen was substantially decreased during AC-2 preparation.

AC-1 and AC-2 were subjected to annular bright-field scanning transmission electron microscopy (ABF-STEM) measurements. In these experiments, weak spots derived from the lattice oxygen were detected between the dark spots derived from the constituent metals.[26,27] Figure 3b−e shows representative ABF-STEM images of AC-1 and AC-2 captured along the (001) plane (see Figures S6 and S7 for additional images). Oxygen contrasts in the PU (OC_{PU}) and Pen (OC_{Pen}) were measured for 150−200 points, respectively, and were averaged to calculate the OC_{PU}/OC_{Pen} ratio. In these measurements, the intensity of the contrasts increased when the occupancy of lattice oxygen decreased; therefore, a lower OC_{PU}/OC_{Pen} ratio indicates a lower occupancy of OC_{Pen} compared to that of OC_{PU}. For AC-1, the OC_{PU}/OC_{Pen} ratio was 0.86. However, the ratio obtained for AC-2 was 0.81,

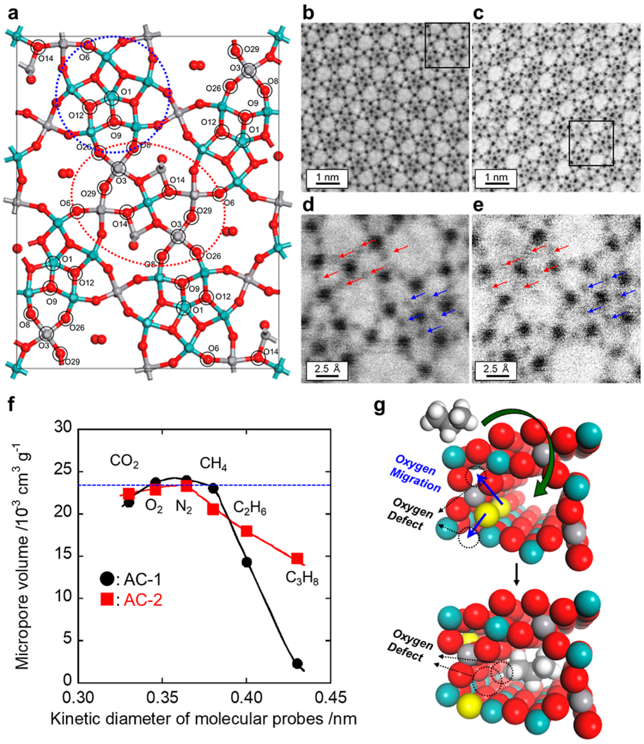

Figure 3. (a) Structural model of MoVO: Mo, green; V, gray; and O, red. PU and Pen are marked by blue and red dotted circles. The lattice oxygens presenting an occupancy decrease of >5% when preparing AC-2 are marked by black circles. (b−e) ABF-STEM images of AC-1 (b,d) and AC-2 (c,e). Black enclosure in (b,c) is expanded to present (d,e). The red and blue arrows in (d,e) indicate the sites of lattice oxygen in Pen and PU, respectively. (f) Micropore volumes of AC-1 and AC-2 were measured using various probe molecules. The blue dotted line indicates the theoretically calculated micropore volume of an empty heptagonal channel (23.4×10^{-3} cm^3 g^{-1}). (g) Diagram of lattice oxygen migration around the heptagonal channel upon molecule entry. Mo, green; V, gray; O, red; C, gray; and H, white. Migrated oxygen atoms are shown in yellow for better understanding.

which was slightly lower than that for AC-1. This statistical estimation implies that the occupancy of lattice oxygen constituting Pen preferentially decreased when preparing AC-2.

Based on the results of the ND and ABF-STEM measurements, we found that Pen preferentially generated lattice oxygen defects when preparing AC-2, which would relate to α-oxygen defects. As Pen constitutes the heptagonal channel micropore as the catalysis field for the ODHE, we investigated the microporosities of AC-1 and AC-2. Adsorption experiments were conducted using probe molecules with kinetic diameters ranging from 0.33 nm (CO$_2$) to 0.43 nm (propane).[14] The resulting adsorption isotherms are presented in Figure S8. As reported previously, AC-1 and AC-2 showed adsorption properties for these molecules, although HT-1 showed almost no adsorption.[11] Figure 3f presents the micropore volumes of AC-1 and AC-2 measured using various probe molecules as a function of their kinetic diameter. For AC-1, molecules with a size smaller than methane (0.38 nm) were adsorbed up to the theoretically calculated micropore volume of the empty heptagonal channel (23.4×10^{-3} cm^3 g^{-1}).[11] However, the amount of micropore adsorption decreased when ethane (0.40 nm) was used, and this was almost negligible when propane was used (0.43 nm). By contrast, AC-2 adsorbed a substantial amount of propane (14.8×10^{-3} cm^3 g^{-1}), indicating that α-oxygen removal expands the heptagonal channel micropore size enough to adsorb propane.

As the ND and ABF-STEM measurements implied, α-oxygen defects are preferentially distributed within Pen in AC-2. The adsorption experiments indicated an expansion of the heptagonal channel with α-oxygen removal. Based on these results, we propose that lattice oxygen migration occurs upon molecule entry into the heptagonal channel owing to changes in the bond length or its angle around the micropore (Figure 3g). This migration leads to oxygen defect localization at the site of the bridging oxygen in the Pen facing the heptagonal channel, resulting in the expansion of the micropore. Considering the quantity of this lattice oxygen (4/unit cell) and that of the lattice oxygen irreversibly removed during the preparation of AC-2 (3.2−3.3/unit cell), approximately 80% of these lattice oxygen sites become vacant when molecules enter the heptagonal channel micropore.

Electronic Structure of MoVO after α-Oxygen Removal and Active Oxygen Species. Next, we investigated the electronic structure of MoVO after α-oxygen removal by DFT calculations using the periodic crystal structure (see Supporting Information for details of crystal structure modeling).

DFT calculations results obtained using the structural model devoid of V = O in the hexagonal channel are summarized in Table 1 and Figure 4, and the corresponding electronic structures are presented in Figure S9. For the structural model containing no lattice oxygen defects (fresh model, Figure 4a), Mo at the center of Pen (Mo29) and Mo and V in Pen facing the heptagonal channel (Mo25 and V4) had Bader charges of 2.39e$^-$, 2.39e$^-$, and 2.00e$^-$, respectively, and their spin densities were negligible (Table 1). Thereafter, the bridging oxygen in the Pen facing the heptagonal channel was removed to create an α-oxygen defect (defect model, Figure 4b). The Bader charges and spin densities were not significantly different in Mo29 and V4. However, the Bader charge in Mo25 decreased to 2.04e$^-$, and the spin density was increased to

Table 1. Physicochemical Properties of Metals and Oxygen Around the Heptagonal Channel in the Model in the V = O Absence Model

structural model	E_{O2}/kcal mol−^{1}	O105−O109 distance/Å	Bader charge					spin density				
			Mo25	V4	Mo29	O105	O109	Mo25	V4	Mo29	O105	O109
fresh			2.39	2.00	2.39			0.01	0.02	0.00		
defect			2.04	1.91	2.48			1.78	0.03	0.15		
molecular O$_2$	0.0	1.23	2.05	1.93	2.44	−0.00	−0.01	1.77	0.03	0.17	1.00	0.99
superoxo	−18.7	1.31	2.28	1.96	2.37	−0.08	−0.40	0.82	0.02	0.14	0.68	0.33
peroxo	−31.4	1.42	2.42	1.93	2.51	−0.29	−0.47	0.004	0.02	0.00	0.001	0.001

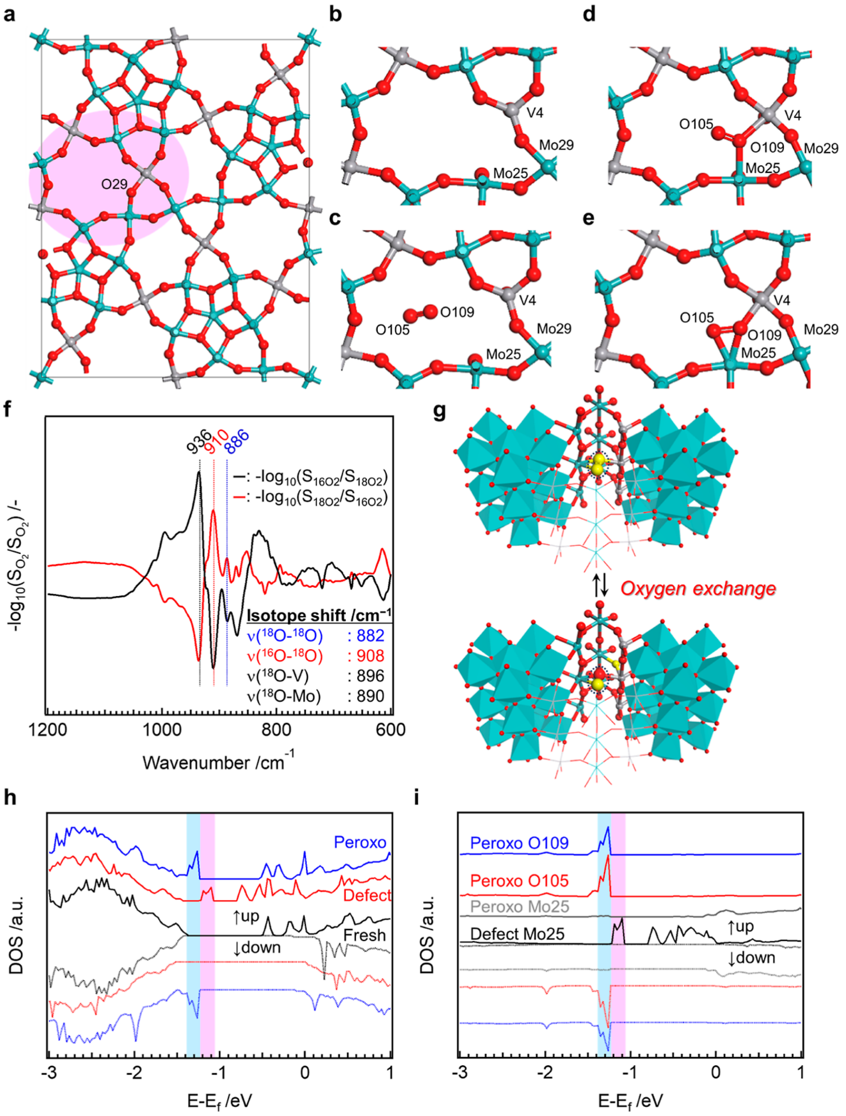

Figure 4. (a) Structural model of MoVO in the absence of V = O in the hexagonal channel containing no lattice oxygen defects (fresh model). The local structure around the heptagonal channel micropore is marked in pink. (b−e) Local structure around the heptagonal channel in the defect (b), molecular O_2 (c), superoxo (d), and peroxo models (e). (f) Difference in IR spectra recorded under flowing $^{16}O_2$/He or $^{18}O_2$/He (1/79 mL min^{-1}). Gas switching order: black line, He → $^{16}O_2$/He → $^{18}O_2$/He; red line, He → $^{18}O_2$/He → $^{16}O_2$/He. IR band at 936 cm^{-1} was attributed to $\nu(^{16}O-^{16}O)$ for the calculations of isotope shift. g Images of oxygen exchange. PU is shown as a polyhedron in this manner for better understanding. Mo, green; V, gray; ^{16}O, red; and ^{18}O, yellow. (h,i) DOS (h) and partial DOS (i) plots of the fresh, defect, and peroxo models.

1.78, indicating the localization of nearly two electrons on Mo25. Then, molecular oxygen (O105 = O109) was introduced into the heptagonal channel in the defect model. Three structural models were obtained after geometry optimizations: (1) molecular oxygen without activation (molecular O_2 model, Figure 4c), (2) molecular oxygen activated as superoxo (superoxo model, Figure 4d), and (3) molecular oxygen activated as peroxo (peroxo model, Figure 4e). The O−O distances were consistent with those of the corresponding oxygen species (Table 1).[28,29] Among these structural models, the peroxo model was the most stable, and the interaction energy between the oxygen molecule and the heptagonal channel (E_{int}) was calculated to be −31.4 kcal mol_{O2}^{-1} as compared with the molecular O_2 model. In the molecular O_2 model, the Bader charges, and spin densities were almost the same as those in the defect model. However, the Bader charge of Mo25 increased with a decrease in the spin density in the superoxo model, and these changes became more pronounced in the peroxo model. In the peroxo model, the Bader charge and spin density of Mo25 were 2.42e$^-$ and 0.004, respectively, indicating the disappearance of electrons localized on Mo25.

For the oxygen molecule introduced into the heptagonal channel (O105 and O109), the Bader charges were almost zero, and the spin densities were almost one in the molecular O_2 model, indicating the biradical nature.[30] However, the Bader charge increased with a decrease in the spin density in the superoxo model, and this trend was more striking in the peroxo model. The Bader charges and spin densities of O105 and O109 in the peroxo model were −0.29e$^-$ and −0.47e$^-$ and 0.001 and 0.001, respectively, indicating the gain of electrons. According to these results, we concluded that the electrons localized on Mo25 were transferred to molecular oxygen to generate peroxo. Note that the Bader charges of the lattice oxygens in the framework structure were in the range of −0.62−−0.95, and these values were substantially lower than

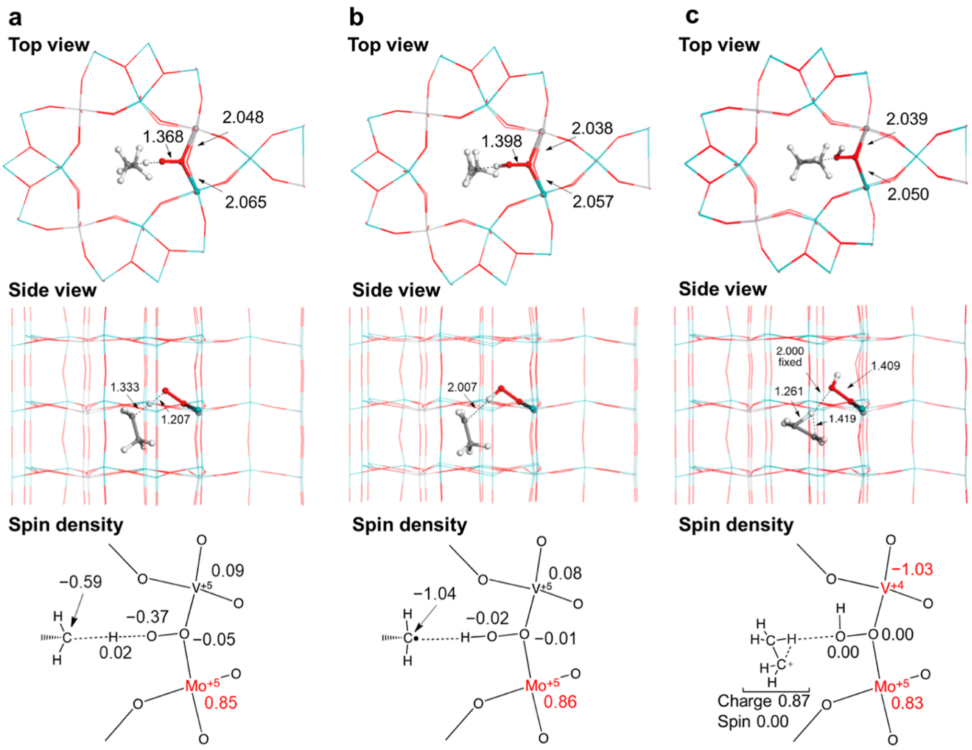

Figure 5. Values presented in the top and side views indicate the distance, and those presented in the spin density view indicate the spin density. (a) Transition state of hydrogen atom abstraction by peroxo. An electron was transferred to adjacent Mo. (b) Hydrogen atom abstraction from ethane while leaving the ethyl radical. (c) Structural image of a second hydrogen atom abstraction. To represent the molecular structure during the hydrogen abstraction, the O−H distance was fixed at 2.000 Å. The cation intermediate formed three-center, two-electron bonding.

those for peroxo, implying that peroxo has an electrophilic nature.[31] Almost the same conclusion was drawn for the structural model containing V = O in the hexagonal channel (Table S2 and Figure S10). It is important to note that when molecular oxygen transforms into lattice oxygen, four-electron reduction is necessary ($O_2 + 4e^- \rightarrow 2O^{2-}$). In the current case, the molecular oxygen can gain only two electrons at the defect since electrons are localized on the defect-adjacent metals. This electron localization could account for the irreversible removal of α-oxygen during the redox treatments.

To experimentally confirm the generation of peroxo, we conducted in situ IR experiments using molecular oxygen isotopomers over AC-2. The IR spectra obtained in the presence/absence of oxygen are shown in Figure S11a−d. Figure 4f presents the difference in IR spectra obtained upon isotope gas switching. Irrespective of the order of the isotope gas switching, an isotope shift was observed from 936 cm^{-1} ($^{16}O_2$/He flow) to 910 and 886 cm^{-1} ($^{18}O_2$/He flow). If the IR band of $\nu(^{16}O-^{16}O)$ was to be assigned to 936 cm^{-1}, the IR bands of $\nu(^{16}O-^{18}O)$ and $\nu(^{18}O-^{18}O)$ would appear at 908 and 882 cm^{-1}, respectively. These values are consistent with those observed experimentally (910 and 886 cm^{-1}). Vibrational frequencies were then calculated by DFT calculations, and the results obtained are summarized in Table S3. The frequency ranges of ν(O−O) in the molecular O_2, superoxo, and peroxo models were calculated to be 1555−1558, 1107−1138, and 950−970 cm^{-1}, respectively, which lies in the typical frequency range of the corresponding oxygen species.[28,29,32,33] The calculated frequency range of peroxo ν(O−O) was close to the experimentally observed IR band position (936 cm^{-1}). Based on these results, we assigned the experimentally obtained IR band to peroxo. Notably, the IR band at 910 cm^{-1} was more pronounced than that at 886 cm^{-1}, indicating that $\nu(^{16}O-^{18}O)$ is the major species after isotope gas switching. We speculate that the oxygen atom in $^{18}O-^{18}O$ peroxo formed at the α-oxygen defect can be replaced with the lattice oxygen to form $^{16}O-^{18}O$ peroxo during the lattice oxygen migration process as proposed above (Figure 4g).

DOS plots were drawn to investigate the electronic states. Figure 4h presents the DOS plots of the fresh (Figure 4a), defect (Figure 4b), and peroxo (Figure 4e) models, and the partial DOS plots are presented in Figure 4i. In the fresh model, a band gap was observed within the $E-E_f$ range of −1.4−−0.5 eV. Upon the formation of the lattice oxygen defect, a new electron level appeared at $E-E_f = -1.1$ eV. The partial DOS plot indicated that this new electron level was associated with the Mo 4d orbital of Mo25. This electron level disappeared upon the formation of peroxo, and a new electron level appeared at the highest occupied molecular orbital. This electron level was associated with peroxo, as demonstrated by the partial DOS plot, implying that peroxo could act as a catalytically active oxygen species.

Oxidation Catalysis of MoVO for the ODHE. We then conducted DFT calculations for the ODHE using the periodic electrostatic embedded cluster model.[34] A structural image of the used cluster is presented in Figures S12 and S13, and the physicochemical properties obtained by the calculations are summarized in Table S4.

Different from the DFT calculations conducted using the periodic crystal structure, two electrons were distributed across the Mo and V atoms adjacent to the defect (Table S4). This difference would be derived from the electronic interaction with axial metals since the defect site was created only at the third layer among the five layers. Upon the introduction of

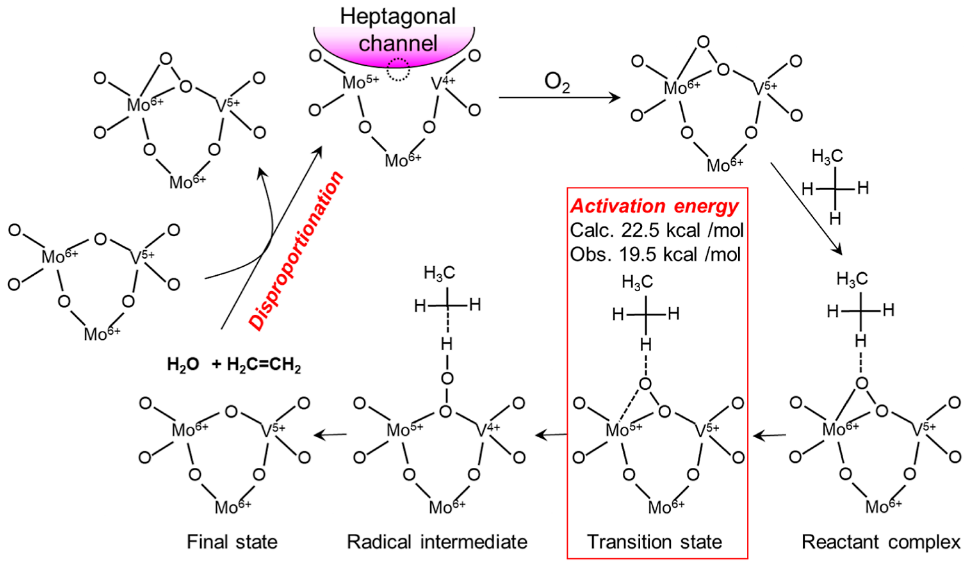

Figure 6. Reaction scheme of the ODHE over MoVO inside the heptagonal channel micropore. α-Oxygen defects are marked by a dotted circle. C−H abstraction from ethane is the rate-determining step.

molecular oxygen, the molecular O_2, superoxo, and peroxo models were obtained after geometry optimizations (Figure S13), and the peroxo model was the most stable among them (Table S4). The E_{int} values, O−O distances, and spin densities were consistent with those obtained using the periodic structure system (Tables 1, S2, and S4). Electrons localized on the defect-adjacent metals almost disappeared upon the formation of peroxo, accompanied by an increase in their spin density, indicating that the electron transfer occurs from the metals to the oxygen molecule.

Thereafter, an ethane molecule was introduced into the cluster model, and transition state calculations were conducted. Representative states are shown in Figure 5 and the entire calculation results are presented in Figure S14. The ethane molecule entered the channel vertically and established close contact with peroxo. The ethane C−H bond was radically abstracted by peroxo, and a spin density of −0.59 was left on the resulting carbon (Figure 5a). At this moment, the Mo binding with peroxo should gain the electron, as the barrier height in this process (Mo-reduced form, 22.5 kcal mol^{-1}) is favored over that when V gains the electron (V-reduced form, 24.2 kcal mol^{-1}). After the hydrogen atom was abstracted, the spin densities of C and Mo were −1.04 and +0.86, respectively (Figure 5b). The resultant radical intermediate was then subjected to a second hydrogen abstraction. In this case, electron transfer from the ethyl radical to V^{5+} proceeded as an exothermic process, and the resultant cation intermediate variously collapsed into the final product. During this process, the second hydrogen atom was abstracted through proton-coupled electron transfer instead of the standard hydrogen atom transfer, resulting in the reduction of V (spin density: −1.03). It is noted that the reaction intermediate stabilized to create a triangular shape by establishing three-center, two-electron bonding, as presented in Figure 5c. Finally, ethylene and water were produced through a highly exothermic process with a barrier height of −57.3 kcal mol^{-1}.

In this reaction scheme, the first hydrogen abstraction is the rate-determining step with a barrier height of 22.5 kcal mol^{-1}. It is worth noting that the apparent activation energy during ODHE over AC-2 was 19.5 kcal mol^{-1}, which was consistent with the calculated barrier height (Figure S15). This consistency strongly supports the validity of this reaction scheme. The activation energy of AC-1 was 19.3 kcal mol^{-1}, and this value was comparable to that of AC-2. The difference in the catalytic activity was solely derived from the pre-exponential factor, which was 0.87×10^9 mmol s^{-1} $g_{cat}{}^{-1}$ and 2.20×10^9 mmol s^{-1} $g_{cat}{}^{-1}$ for AC-1 and AC-2, respectively, presenting a 2.5-fold difference. Therefore, the difference in the catalytic activity between AC-1 and AC-2 is derived from the number of lattice oxygen defect sites responsible for molecular oxygen activation.

Figure 6 summarizes the reaction mechanism. When molecular oxygen was introduced into the α-oxygen defect, peroxo was generated. With the introduction of ethane, the hydrogen atom was abstracted by peroxo, leading to the formation of a radical intermediate. After the second hydrogen abstraction, ethylene and water were generated. During this process, the intermediate was stabilized through three-center, two-electron bonding. The oxygen atom left at the α-oxygen defect site could be disproportionate to regenerate the α-oxygen defect site and peroxo.[35]

■ CONCLUSIONS

We clarified the oxidation catalysis of MoVO, a promising catalyst for ODHE. The catalytic activity of MoVO drastically increased with appropriate redox treatments, which irreversibly removed specific lattice oxygens from the crystal structure. Upon molecule entry into the heptagonal channel, such defects were concentrated at the site facing the heptagonal channel in Pen through lattice oxygen migration. Electrons were localized on the metals adjacent to the resulting oxygen defects. These electrons were transferred to molecular oxygen upon its introduction, generating electrophilic peroxo as the catalytically active oxygen species. We concluded that catalytically active species in MoVO are generated by the sophisticatedly organized local structure involving oxygen defects. This work provided a fundamental understanding of oxidation chemistry, paving the way to develop evolution-based oxidation catalysts.

ASSOCIATED CONTENT

Supporting Information

The Supporting Information is available free of charge at https://pubs.acs.org/doi/10.1021/acscatal.3c04591.

> Experimental details; structural properties and catalytic activities over MoVO and MoVTeNbO; XRD patterns of AC-1, HT-1, and AC-2; reaction rates of ethane and propane oxidation as functions of the contact time over AC-1 and AC-2; TG−DTA profiles of AC-1, HT-1, and AC-2 measured under an oxidation/reduction atmosphere; results of Rietveld refinements; HAADF-STEM and ABF-STEM images of AC-1 and AC-2; adsorption isotherms of AC-1, HT-1, and AC-2; electronic structure of MoVO in the absence/presence of V = O in the hexagonal channel; difference IR spectra recorded in the presence/absence of $^{16}O_2$ or N_2; structure of the cluster models; detail reaction scheme for the ODHE; Arrhenius plot for the ODHE over AC-1 and AC-2; structural model of MoVO determined by the single crystal analyses; physicochemical properties and results of the ODHE for AC-1, HT-1, and AC-2; physicochemical properties of metals and oxygen around the heptagonal channel in the V = O containing model; results of vibration calculations; physicochemical properties of metals and oxygen around the heptagonal channel in the cluster model; and results of Rietveld refinements for AC-1 and AC-2 using ND (SE) patterns (PDF)

AUTHOR INFORMATION

Corresponding Authors

Satoshi Ishikawa − *Department of Applied Chemistry, Faculty of Chemistry and Biochemistry, Kanagawa University, Yokohama 221-8686, Japan;* orcid.org/0000-0003-4372-4108; Email: sishikawa@kanagawa-u.ac.jp

Wataru Ueda − *Department of Applied Chemistry, Faculty of Chemistry and Biochemistry, Kanagawa University, Yokohama 221-8686, Japan*; Email: uedaw@kanagawa-u.ac.jp

Authors

Kosuke Shimoda − *Institute for Catalysis, Hokkaido University, Sapporo 001-0021, Japan*

Takashi Kamachi − *Department of Life, Environment and Applied Chemistry, Fukuoka Institute of Technology, Fukuoka-shi, Fukuoka 811-0295, Japan;* orcid.org/0000-0001-9281-0454

Nagisa Aoki − *Department of Applied Chemistry, Faculty of Chemistry and Biochemistry, Kanagawa University, Yokohama 221-8686, Japan*

Takeshi Hagiwara − *Research Institute for Engineering, Kanagawa University, Yokohama 221-8686, Japan*

Atsushi Urakawa − *Catalysis Engineering, Department of Chemical Engineering, Delft University of Technology, Delft 2629 HZ, The Netherlands;* orcid.org/0000-0001-7778-4008

Complete contact information is available at: https://pubs.acs.org/10.1021/acscatal.3c04591

Notes

The authors declare no competing financial interest.

ACKNOWLEDGMENTS

The authors are grateful for the financial support from the JSPS KAKENHI (grant no. 21K14464), the Tokuyama Science Foundation, and the Joint Usage/Research Center for Catalysis (22AY0034). This research was partially conducted at Hokkaido University and is supported by the Nanotechnology Platform Program of the Ministry of Education, Culture, Sports, Science and Technology (MEXT), Japan (grant no. JPMXP09A21HK0040). The neutron experiment at the Materials and Life Science Experimental Facility of the J-PARC was performed under a user program (proposal no. 2019BM0024).

REFERENCES

(1) Gärtner, C. A.; van Veen, A. C.; Lercher, J. A. Oxidative Dehydrogenation of Ethane: Common Principles and Mechanistic Aspects. *ChemCatChem* **2013**, *5*, 3196−3217.

(2) Grant, J. T.; Venegas, J. M.; McDermott, W. P.; Hermans, I. Aerobic Oxidations of Light Alkanes over Solid Metal Oxide Catalysts. *Chem. Rev.* **2018**, *118*, 2769−2815.

(3) Najari, S.; Saeidi, S.; Concepcion, P.; Dionysiou, D. D.; Bhargava, S. K.; Lee, A. F.; Wilson, K. Oxidative Dehydrogenation of Ethane: Catalytic and Mechanistic Aspects and Future Trends. *Chem. Soc. Rev.* **2021**, *50*, 4564−4605.

(4) Valente, J. S.; Quintana-Solórzano, R.; Armendáriz-Herrera, H.; Millet, J.-M. M. Decarbonizing Petrochemical Processes: Contribution and Perspectives of the Selective Oxidation of C1-C3 Paraffins. *ACS Catal.* **2023**, *13*, 1693−1716.

(5) Cavani, F.; Ballarini, N.; Cericola, A. Oxidative Dehydrogenation of Ethane and Propane: How Far from Commercial Implementation? *Catal. Today* **2007**, *127*, 113−131.

(6) Nieto, J. M. L.; Botella, P.; Vázquez, M. I.; Dejoz, A. The Selective Oxidative Dehydrogenation of Ethane over Hydrothermally Synthesised MoVTeNb Catalysts. *Chem. Commun.* **2002**, 1906−1907.

(7) Zenkovets, G. A.; Shutilov, A. A.; Bondareva, V. M.; Sobolev, V. I.; Marchuk, A. S.; Tsybulya, S. V.; Prosvirin, I. P.; Ishchenko, A. V.; Gavrilov, V. Y. New Multicomponent $MoVSbNbCeO_x/SiO_2$ Catalyst with Enhanced Catalytic Activity for Oxidative Dehydrogenation of Ethane to Ethylene. *ChemCatChem* **2020**, *12*, 4149−4159.

(8) Annamalai, L.; Ezenwa, S.; Dang, Y.; Tan, H.; Suib, S. L.; Deshlahra, P. Comparison of Structural and Catalytic Properties of Monometallic Mo and V Oxides and M1 Phase Mixed Oxides for Oxidative Dehydrogenation. *Catal. Today* **2021**, *368*, 28−45.

(9) DeSanto, P.; Buttrey, D. J.; Grasselli, R. K.; Lugmair, C. G.; Volpe, A. F.; Toby, B. H.; Vogt, T. Structural Characterization of the Orthorhombic Phase M1 in MoVNbTeO Propane Ammoxidation Catalyst. *Top. Catal.* **2003**, *23*, 23−38.

(10) Konya, T.; Katou, T.; Murayama, T.; Ishikawa, S.; Sadakane, M.; Buttrey, D.; Ueda, W. An Orthorhombic Mo_3VO_x Catalyst Most Active for Oxidative Dehydrogenation of Ethane among Related Complex Metal Oxides. *Catal. Sci. Technol.* **2013**, *3*, 380−387.

(11) Ishikawa, S.; Kobayashi, D.; Konya, T.; Ohmura, S.; Murayama, T.; Yasuda, N.; Sadakane, M.; Ueda, W. Redox Treatment of Orthorhombic $Mo_{29}V_{11}O_{112}$ and Relationships between Crystal Structure, Microporosity and Catalytic Performance for Selective Oxidation of Ethane. *J. Phys. Chem. C* **2015**, *119*, 7195−7206.

(12) Trunschke, A.; Noack, J.; Trojanov, S.; Girgsdies, F.; Lunkenbein, T.; Pfeifer, V.; Hävecker, M.; Kube, P.; Sprung, C.; Rosowski, F.; Schlögl, R. The Impact of the Bulk Structure on Surface Dynamics of Complex Mo-V-based Oxide Catalysts. *ACS Catal.* **2017**, *7*, 3061−3071.

(13) Sadakane, M.; Kodato, K.; Yasuda, N.; Ishikawa, S.; Ueda, W. Thermal Behavior, Crystal Structure, and Solid-State Transformation of Orthorhombic Mo-V Oxide under Nitrogen Flow or in Air. *ACS Omega* **2019**, *4*, 13165−13171.

(14) Sadakane, M.; Kodato, K.; Kuranishi, T.; Nodasaka, Y.; Sugawara, K.; Sakaguchi, N.; Nagai, T.; Matsui, Y.; Ueda, W.

Molybdenum-Vanadium-Based Molecular Sieves with Microchannels of Seven-Membered Rings of Corner-Sharing Metal Oxide Octahedra. *Angew. Chem., Int. Ed.* **2008**, *47*, 2493−2496.

(15) Foppa, L.; Rüther, F.; Geske, M.; Koch, G.; Girgsdies, F.; Kube, P.; Carey, S. J.; Hävecker, M.; Timpe, O.; Tarasov, A. V.; Scheffler, M.; Rosowski, F.; Schlögl, R.; Trunschke, A. Data-Centric Heterogeneous Catalysis: Identifying Rules and Materials Genes of Alkane Selective Oxidation. *J. Am. Chem. Soc.* **2023**, *145*, 3427−3442.

(16) Ishikawa, S.; Yi, X.; Murayama, T.; Ueda, W. Heptagonal Channel Micropore of Orthorhombic Mo_3VO_x as Catalysis Field for the Selective Oxidation of Ethane. *Appl. Catal., A* **2014**, *474*, 10−17.

(17) Ishikawa, S.; Yi, X.; Murayama, T.; Ueda, W. Catalysis Field in Orthorhombic Mo_3VO_x Oxide Catalyst for the Selective Oxidation of Ethane, Propane and Acrolein. *Catal. Today* **2014**, *238*, 35−40.

(18) Ishikawa, S.; Ueda, W. Microporous Crystalline Mo-V Mixed Oxides for Selective Oxidations. *Catal. Sci. Technol.* **2016**, *6*, 617−629.

(19) Ishikawa, S.; Ueda, W. Mo-V-Based Crystalline Complex Metal Oxide Catalysts. In *Crystalline Metal Oxide Catalysts*; Ueda, W., Ed.; Springer Nature: Singapore, 2022; pp 101−121.

(20) Ishigaki, T.; Hoshikawa, A.; Yonemura, M.; Morishima, T.; Kamiyama, T.; Oishi, R.; Aizawa, K.; Sakuma, T.; Tomota, Y.; Arai, M.; Hayashi, M.; Ebata, K.; Takano, Y.; Komatsuzaki, K.; Asano, H.; Takano, Y.; Kasao, T. IBARAKI Materials Design Diffractometer (iMATERIA)-Versatile Neutron Diffractometer at J-PARC. *Nucl. Instrum. Methods Phys. Res., Sect. A* **2009**, *600*, 189−191.

(21) Izumi, F.; Momma, K. Three-Dimensional Visualization in Powder Diffraction. *Solid State Phenom.* **2007**, *130*, 15−20.

(22) Oishi, R.; Yonemura, M.; Nishimaki, Y.; Torii, S.; Hoshikawa, A.; Ishigaki, T.; Morishima, T.; Mori, K.; Kamiyama, T. Rietveld Analysis Software for J-PARC. *Nucl. Instrum. Methods Phys. Res., Sect. A* **2009**, *600*, 94−96.

(23) Asada, T.; Arao, M.; Kubobuchi, K.; Mogi, M.; Takahashi, Y.; Matsumoto, M.; Ishihara, A.; Ota, K.; Imai, H. Determination of Oxygen-Reduction-Reaction Active Sites of Tantalum Oxide-based Cathodes Used for Polymer Electrolyte Fuel Cells. *Fuel Cells* **2014**, *14*, 769−774.

(24) Yashima, M.; Tsujiguchi, T.; Fujii, K.; Niwa, E.; Nishioka, S.; Hester, J. R.; Maeda, K. Direct Evidence for Two-Dimensional Oxide-Ion Diffusion in the Hexagonal Perovskite-Related Oxide $Ba_3MoNbO_{8.5-\delta}$. *J. Mater. Chem. A* **2019**, *7*, 13910−13916.

(25) Yashima, M.; Tsujiguchi, T.; Sakuda, Y.; Yasui, Y.; Zhou, Y.; Fujii, K.; Torii, S.; Kamiyama, T.; Skinner, S. J. High Oxide-Ion Conductivity Through the Interstitial Oxygen Site in $Ba_7Nb_4MoO_{20}$-Based Hexagonal Perovskite Related Oxides. *Nat. Commun.* **2021**, *12*, 556.

(26) Lunkenbein, T.; Girgsdies, F.; Wernbacher, A.; Noack, J.; Auffermann, G.; Yasuhara, A.; Klein-Hoffmann, A.; Ueda, W.; Eichelbaum, M.; Trunschke, A.; Schlögl, R.; Willinger, M. G. Direct Imaging of Octahedral Distortion in a Complex Molybdenum Vanadium Mixed Oxide. *Angew. Chem., Int. Ed.* **2015**, *54*, 6828−6831.

(27) Lunkenbein, T.; Masliuk, L.; Plodinec, M.; Algara-Siller, G.; Jung, S.; Jastak, M.; Kube, P.; Trunschke, A.; Schlögl, R. Site Specific and Localized Structural Displacements in Open Structured Multimetallic Oxides. *Nanoscale* **2020**, *12*, 6759−6766.

(28) Cramer, C. J.; Tolman, W. B.; Theopold, K. H.; Rheingold, A. L. Variable Character of O-O and M-O Bonding in Side-on (η^2) 1:1 metal complexes of O_2. *Proc. Natl. Acad. Sci. U.S.A.* **2003**, *100*, 3635−3640.

(29) Kee, C. W. Assignment of O-O and Mo = O Stretching Frequencies of Molybdenum/Tungsten Complexes Revisited. *J. Chem.* **2015**, *2015*, 1−10.

(30) Machan, C. W. Advances in the Molecular Catalysis of Dioxygen Reduction. *ACS Catal.* **2020**, *10*, 2640−2655.

(31) Ishikawa, S.; Ikeda, T.; Koutani, M.; Yasumura, S.; Amakawa, K.; Shimoda, K.; Jing, Y.; Toyao, T.; Sadakane, M.; Shimizu, K.-i.; Ueda, W. Oxidation Catalysis over Solid-State Keggin-Type Phosphomolybdic Acid with Oxygen Defects. *J. Am. Chem. Soc.* **2022**, *144*, 7693−7708.

(32) Chow, K. K.; Short, M.; Lam, S.; McWilliams, A.; Zeng, H. A Raman Cell Based on Hollow Core Photonic Crystal Fiber for Human Breath Analysis. *Med. Phys.* **2014**, *41*, 092701.

(33) Akita, M.; Moro-oka, Y. Reductive Activation of Dioxygen: A New Concept for the Catalytic Oxidation. *Catal. Today* **1998**, *44*, 183−188.

(34) Burow, A. M.; Sierka, M.; Döbler, J.; Sauer, J. Point Defects in CaF_2 and CeO_2 Investigated by the Periodic Electrostatic Embedded Cluster Method. *J. Chem. Phys.* **2009**, *130*, 174710.

(35) Pierini, A.; Brutti, S.; Bodo, E. Reactive pathways toward parasitic release of singlet oxygen in metal-air batteries. *npj Comput. Mater.* **2021**, *7*, 126.

https://doi.org/10.1021/acscatal.3c04591